Composites: Part A 210 (2026) 110041

Contents lists available at ScienceDirect

Composites Part A

journal homepage: www.elsevier.com/locate/compositesa

Application of energy-efficient electromagnetic Melt-Processing for the upcycling of recycled polyphenylene sulfide into multifunctional segregated nanocomposites

Madara Mohoppu [a,b], Utsab Ayan [a,b], Bibek Kattel [c], Oussama Oulhakem [b], Olivia McNair [d], Ahmed Al-Ostaz [b,e], Enrique Jackson [f], Byron S. Villacorta [a,b,g,*]

[a] Department of Chemical Engineering, University of Mississippi, University, MS 38677, USA
[b] Center for Graphene Research and Innovation (CGRI), University of Mississippi, University, MS 38677, USA
[c] Department of Engineering, University of Southern Indiana, Evansville, IN 47712, USA
[d] School of Polymer Science and Engineering, University of Southern Mississippi, Hattiesburg, MS 39406, USA
[e] Department of Civil Engineering, University of Mississippi, University, MS 38677, USA
[f] Marshall Space Flight Center, National Aeronautics and Space Administration, Huntsville, AL 35808, USA
[g] School of Mechanical and Mining Engineering, University of Queensland, Saint Lucia, QLD 4067, Australia

GRAPHICAL ABSTRACT

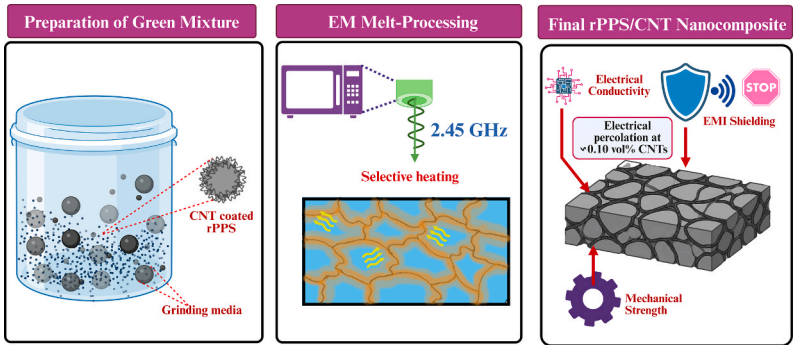

ARTICLE INFO

Keywords:
Electromagnetic melt-processing
Upcycling
Nanocomposites
Polyphenylene sulfide
Carbon nanotubes

ABSTRACT

Polyphenylene sulfide (PPS) is widely used in structural and functional composites because of its thermal stability, chemical resistance, and mechanical strength. As circular manufacturing becomes increasingly important, extending the service life of recycled PPS (rPPS) is essential. However, conventional high-temperature reprocessing accelerates thermo-oxidative degradation, reducing recycled composite performance. This study proposes a rapid and potentially energy-saving upcycling strategy for rPPS using electromagnetic (EM) melt-processing to form segregated carbon nanotube (CNT) networks and produce EM-responsive nanocomposites. The aim was to determine whether CNT-assisted EM heating could reduce polymer degradation while improving multifunctional properties at ultralow filler loadings. rPPS micropellets were coated with CNTs by ball milling to create conductive shells, then compacted into green bodies (GBs) and selectively melted by rapid EM irradiation.

* Corresponding author..
E-mail address: bsvillac@olemiss.edu (B.S. Villacorta).

https://doi.org/10.1016/j.compositesa.2026.110041
Received 31 March 2026; Received in revised form 11 June 2026; Accepted 24 June 2026
Available online 25 June 2026

Structural, electrical, mechanical, rheological, and electromagnetic interference (EMI) shielding properties were evaluated. Electrical percolation occurred at an ultralow CNT loading of 0.08 wt%, with conductivity reaching $(1.24 \pm 0.74) \times 10^{-5}$ S·m^{-1} at 0.1 wt%. At this concentration, tensile strength and modulus increased by 72% and 99%, respectively. At ~ 0.7 mm thickness, X-band EMI shielding effectiveness reached 6 dB for GBs and 3 dB after EM processing. This shows that EM melt-processing upcycles rPPS into high-performance multifunctional nanocomposites with minimum thermal degradation.

Introduction

The growing demand in the aerospace, space, automotive, and energy industries is driving the use of high-temperature polymers that combine lightweight and functional properties with robust mechanical strength under extreme conditions [1,2]. High-performance (HP) thermoplastics, e.g., polyphenylene sulfide (PPS), polyetheretherketone (PEEK), poly(aryl ether ketone) (PAEK), and polyetherimide (PEI), have emerged as preferred candidates for advanced polymer engineering applications due to their exceptional properties and performance [1]. PPS is at the forefront of engineering and high-temperature applications and is a promising candidate among HP polymeric materials. Chemically speaking, PPS is a semi-crystalline thermoplastic polymer consisting of alternating sulfur atoms and aromatic rings, a molecular structure that imparts several desirable properties [3]. These include exceptional chemical and thermal stability [4], inherent flame resistance [5], high heat deflection temperature, and excellent dimensional stability [6]. PPS further distinguishes itself by offering high mechanical performance, favorable electrical insulation, and an intermediate cost relative to other HP thermoplastics [7].

Notably, although pristine PPS is electrically insulating, it can exhibit semiconducting behavior through oxidation or doping, positioning it as a potential precursor for semi-flexible conducting polymers [8]. To further expand its functional range, conductive nanofillers, such as carbon nanotubes (CNTs), graphene, and their derivatives, have been incorporated to enhance its electrical, mechanical, and thermal properties [9]. CNTs, in particular, are ideal one-dimensional conductive nanofillers owing to their high axial electrical conductivity (10^4-10^5 S/cm), thermal conductivity (3000–6600 W/m·K), carrier mobility (1000–4000 cm^2/V·s), and exceptional Young's modulus (0.27–1.25 TPa) combined with thermal stability up to 700 °C in air [9–11]. Moreover, strong π-π interactions between the CNT sidewalls and the aromatic rings of PPS promote effective interfacial adhesion, thereby improving stress transfer and load-bearing capability [12].

While CNTs offer exceptional electrical, thermal, and mechanical properties that make them ideal reinforcements in PPS matrices, their practical utilization is hindered by several processing challenges. The high temperatures (300–350 °C) and shear stresses required during conventional melt-mixing and injection molding often induce oxidation and degradation of the PPS matrix [13]. Furthermore, achieving uniform CNT dispersion remains a major challenge, as van der Waals forces drive agglomeration and limit electrical percolation efficiency [14]. Consequently, CNT/PPS thermoplastic nanocomposites (TPNCs) processed via traditional routes typically demand relatively high levels of filler loading (≥4 wt%) to achieve measurable electrical conductivity, which adversely affects mechanical integrity and processability [15]. To overcome these limitations, innovative processing strategies capable of achieving structuring in the nanocomposites are needed to simultaneously attain segregated, but interconnected conductive architectural networks, which will lead to superior functionality at reduced nanoparticle content [16,17].

Recently, electromagnetic (EM) or microwave-assisted melt-processing of thermoplastics has emerged as a sustainable alternative for polymer welding, bonding, sintering, and even melt processing [17–21]. By applying volumetric heating via microwave or radio wave radiation, these techniques achieve rapid and selective surface and/or bulk melting, reducing overall processing times and energy consumption by up to 70–90% compared to conventional heating methods [22–24]. However, the high crystallinity (>45%) and dielectric constant of PPS (3.3–3.9) make it inherently microwave-transparent, restricting dipole rotation, yielding negligible microwave heating [18,25]. Although PPS is intrinsically a low dielectric constant polymer, its slight but finite dielectric loss at high frequencies combined with the conduction loss provided by carbon fillers can still contribute, to some extent, to an efficient heat induction in carbon/PPS composites, where synergistic conductive and dielectric losses generate localized 'hot spots' within the material [26]. This is important when it comes to segregated nanocomposites, where CNTs get strategically positioned, forming an interconnected network, which enables selective heating of the CNT network and of the polymer-CNT interphase zone. This leads to interfacial and bulk polymer melting as well as enhanced polymer-CNT adhesion without exposing the entire matrix to prolonged high temperatures [17,27,28]. As a result, EM melt-processing provides a unique pathway to engineer segregated, interconnected conductive networks in PPS-based nanocomposites while suppressing thermo-oxidative degradation.

Building on these advances, the sustainable use of recycled PPS (rPPS) has become increasingly important as PPS waste generated by high-value manufacturing processes, including injection molding, machining, composite fabrication, and disposed electronics, becomes more widely available [6,29]. Unlike commodity plastics, PPS scrap primarily originates from post-industrial sources, yielding relatively clean but structurally degraded feedstocks that are often downcycled or discarded despite their intrinsic value [30]. Conventional thermal reprocessing of PPS requires prolonged exposure to high temperatures (≥300 °C), which accelerates thermo-oxidative degradation, reduces molecular weight, and compromises mechanical and functional performance [6]. As a result, existing recycling approaches are largely unable to preserve the performance required for advanced engineering applications, highlighting a critical need for upcycling strategies that both mitigate degradation and enable functional enhancement. Although EM melt-processing has demonstrated potential for selective heating and improved polymer-nanofiller interactions [19,31], its application to recycling and even upcycling highly crystalline polymers such as PPS remains insufficiently explored. In particular, the challenge lies in achieving controlled interfacial activation and conductive network formation without inducing bulk thermal damage to the recycled matrix.

Therefore, in this study, we introduce electromagnetic melt-processing as an innovative strategy for the upcycling of recycled PPS (rPPS). This approach utilizes localized microwave heating to trigger interfacial and bulk polymer melting, enhanced adhesion between the polymer and nanofillers, and facilitate the formation of segregated conductive networks confined to micropellet interfaces. By harnessing EM-induced hotspot generation and interfacial activation, the method allows for precise network structuring while minimizing bulk polymer degradation, ultimately improving the functional and mechanical performance of rPPS-based nanocomposites.

Experimental

Materials

Recycled polyphenylene sulfide (rPPS) micropellets, obtained as post-industrial waste from Fortron® 0320-PPS supplied by Celanese Corporation (Irving, TX, USA), were used as the polymer matrix. The

material exhibited a density of 1.35 g·cm^{-3}, a melting point of 283 °C, and a glass transition temperature (T_g) of approximately 90 °C, as determined by differential scanning calorimetry (DSC). Prior to processing, the rPPS micropellets were dried at 120 °C under vacuum for 12 h to remove residual moisture and minimize thermo-oxidative and hydrolytic degradation during melt processing.

Commercial NC7000 multi-walled CNTs, by Nanocyl S.A., Belgium, were employed as the conductive nanofiller. NC7000 possesses a purity of > 90 %, a nominal average outer diameter of ~ 9.5 nm, an average length of 1.5 μm, and a specific surface area of approximately 240 $m^2 \cdot g^{-1}$. The CNTs were used as received without further modification or purification (i.e., pristine).

Ball milling powder Formulation and green bodies Preparation

The rPPS micropellets and CNT nanopowder were mixed using a dry-powder soft ball milling process, following a protocol previously reported [17,32] using a high-energy planetary ball mill (MSE PRO 4 L, MSE Supplies, USA) at 200 rpm and 60 min to obtain uniformly CNT-coated rPPS micropellets at selected filler loadings of 0.1–1.5 wt% and minimizing CNT damage.

Then, the mixtures (here called "green" mixtures) were mechanically compacted at 16 tons for 2 min at room temperature using a hydraulic laboratory press (Carver Model 4389 MHC) and a 40-mm diameter Pellet Pressing Die Set (MSE Supplies) to produce consolidated green bodies (GBs) weighing approximately 0.7 g and a thickness of 0.6–0.8 mm. No external heating was applied during compaction, preserving the as-coated segregated CNT configuration prior to processing. Here, "GB" refers to the mechanically compacted CNT/rPPS mixture before EM melt-processing.

EM melt-processing of nanocomposites

The EM melt-processing of the formulated GBs was carried out in a customized laboratory microwave oven with a True-to-Power® magnetron (Microwave Research & Applications BP-095 UMISS, 2.45 GHz) at 500–900 W for less than 180 s, depending on the GBs' electromagnetic susceptibility, as described previously [17,32]. For the highly crystalline rPPS matrix, effective EM coupling and full polymer melting occurred at loadings ≥ 0.1 wt% CNTs, leading to dense, well-fused "monolithic" nanocomposites. The resulting CNT/rPPS TPNCs were successfully produced at 0.1, 0.3, 0.5, 1.0, and 1.5 wt% and subsequently characterized in terms of morphological, microscopical, electrical, rheological, and electromagnetic properties.

Testing and characterization

Mechanical tensile testing

Tensile testing was carried out for all prepared nanocomposite concentrations. TPNC dogbone specimens were cut out from the processed specimens using a standard die cutter for tensile testing. For this, the ISO 37 standard guidelines were followed, as it includes one of the smallest dogbone standard geometries. Thus, dogbone specimens approximately 300 μm thick were prepared using an ISO 37 Type 4-certified cutting die (Qualitest). Mechanical testing was conducted using a universal testing machine (Instron 5982, Instron, USA) equipped with a 5 kN load cell (Instron 2580 series). Tests were performed at a constant crosshead speed of 1 mm.min^{-1} (A relatively low crosshead speed was selected to ensure stable quasi-static loading and accurate strain tracking for the thin dogbone specimens, while minimizing grip slippage and premature failure during testing), and data acquisition was handled using Bluehill Universal software (Instron). Axial strain was measured using a non-contact video extensometer (Instron Model 2663–902) with a spatial resolution of 5 μm, ensuring accurate strain measurement throughout the test. All experiments were carried out under ambient laboratory conditions (~25 °C and ~ 50 % relative humidity). For each composite formulation, 8–10 specimens were tested to ensure reproducibility. The modulus, ultimate tensile strength, and elongation-at-break were extracted from the resulting stress–strain curves.

Scanning electron Microscopy (SEM)

The morphological and microstructural features of the CNTs, rPPS micropellets, powder formulations, GBs, and EM-processed TPNCs were characterized using a JEOL JSM-7200 FLV field-emission scanning electron microscope (FE-SEM) operated at an accelerating voltage of 3 kV and 15 kV under secondary electron imaging mode. All samples were vacuum-dried prior to analysis to remove residual moisture. Cryo-fractured surfaces of the nanocomposites were mounted on aluminum stubs and sputter-coated with a thin Au/Pd (60/40) alloy film for 60 s using a Denton Desk V TSC coater to minimize charging. For selected analyses, higher accelerating voltages (10–15 kV) were used to resolve filler dispersion and interfacial features.

Electrical conductivity

The through-thickness volume electrical conductivity (σ) of rPPS, GBs, and TPNCs was measured using a Keithley 6517B electrometer paired with a custom-fabricated guarded resistance test fixture (Fig. S1) that complies with ASTM D257. Disc-shaped specimens with flat parallel surfaces were used for the electrical conductivity measurements. During testing, each specimen was placed between the guarded electrodes, with the electrodes contacting the opposite flat faces of the disc. Therefore, the measured resistance corresponded to through-thickness, or out-of-plane, conduction across the specimen thickness. The fully shielded and grounded test fixture allowed voltages from 0.05 V to 1000 V and achieved a current resolution in the picoampere range. The KickStart software was used to apply the alternating polarity method to prevent charge-accumulation artifacts and thermal noise during measurements.

Five GB replicates and five TPNC replicates (specimens) were tested at each CNT loading. For each specimen, three consecutive readings were taken and averaged to ensure statistical reliability of the measurement. Environmental relative humidity (RH) was monitored and remained near 50% RH during testing. The conductivity was calculated using Equation (1):

$$\sigma = \frac{l}{RA} \tag{1}$$

where l is the specimen thickness, R the measured resistance, and A the electrode contact area.

Electromagnetic Interference Shielding Effectiveness (EMI SE).

The EMI SE of the GBs and TPNCs was assessed using an Agilent N5242A vector network analyzer (VNA) equipped with an X-band (8.2–12.4 GHz) WR-90 waveguide setup. Prior to measurement, the system was calibrated using the TRL (Through-Reflect-Line) two-port method to eliminate systematic errors associated with reflections and transmissions. Each sample (~0.6–0.8 mm thick) was cut precisely to match the waveguide aperture and mounted between the flanges of the test fixture. The VNA recorded scattering parameters (S_{11} and S_{21}) for both the load specimen and the reference specimen [17]. The obtained S-parameters were used to compute the EMI SE according to Equation (2):

$$\begin{aligned} EMI\,SE &= -10\log\frac{P_{load}}{P_{ref}} = -10\log\frac{P_{load}}{P_0} + 10\log\frac{P_{ref}}{P_0} \\ &= -10\log\left(|S_{21}|^2_{load}\right) + 10\log\left(|S_{21}|^2_{ref}\right) \end{aligned} \tag{2}$$

Where P_0 denotes the incident power measured coming from the transmission line, while P_{load} and P_{ref} represent the transmitted power through the load and reference specimens, respectively. The measured

scattering parameters (S_{11} and S_{21}) were then used in Equations (3–5) to calculate the reflected (R), transmitted (T), and absorbed (A) power fractions, enabling the determination of both the reflective (EMI SE_R) and absorptive (EMI SE_A) components of the total EMI SE.

$$R = |S_{11}|^2 \tag{3}$$

$$T = |S_{21}|^2 \tag{4}$$

$$A = 1 - |S_{11}|^2 - |S_{21}|^2 \tag{5}$$

Rheological characterization

The time-dependent and dynamic shear viscosity data of the rPPS, GBs, and TPNCs were evaluated using a TA Instruments DHR-2 rotational rheometer equipped with a parallel-plate geometry (25 mm diameter). Prior to testing, all the materials were cut into 25 mm circular discs to ensure uniform contact between plates. A sample thickness of 0.6–0.8 mm was maintained for all tests. Excess material from between the plates during loading was carefully trimmed with a blade to avoid edge effects, and a gap of 0.5 to 0.7 mm was utilized for all tests. Three replicates were tested per CNT loading.

a) Transient shear testing

Transient shear measurements were performed at 320 °C, a temperature well above the melting point of rPPS to ensure complete melting. The specimens were carefully centered on the lower plate of the fixture and trimmed after closing the gap to 0.5–0.7 mm to avoid edge effects. Before each test, the sample was equilibrated at 320 °C for 2 min under a small normal force to eliminate thermal gradients and relax any residual stresses induced during loading. Start-up of steady shear experiments was then carried out at constant shear rates of 0.3, 0.5, and 1.0 s^{-1}, applied sequentially on the same specimen from the lowest to the highest rate without intermediate unloading; each step was maintained for 300 s to capture the full transient stress–growth and viscosity response associated with CNT network distortion, breakage, and partial regeneration.

b) Oscillatory Time-Sweep testing

Dynamic shear rheological measurements were also performed at 320 °C in the linear viscoelastic region (LVR) of the materials. The LVR was predefined through strain-sweep tests (0.01–10 %) at a frequency of 1 Hz. Time-sweep experiments were then performed at 1 % strain and 1 Hz frequency for 40 min to monitor the evolution of the storage modulus (G') and loss modulus (G'') with time. These measurements enabled identification of gel-like transitions, CNT network formation, and crystallization-assisted elasticity in the rPPS matrix.

RESULTS AND DISCUSSION

Microstructure

As displayed in Fig. 1, the morphology of the rPPS micropellets, before and after dry mixing with CNTs, was characterized by SEM.

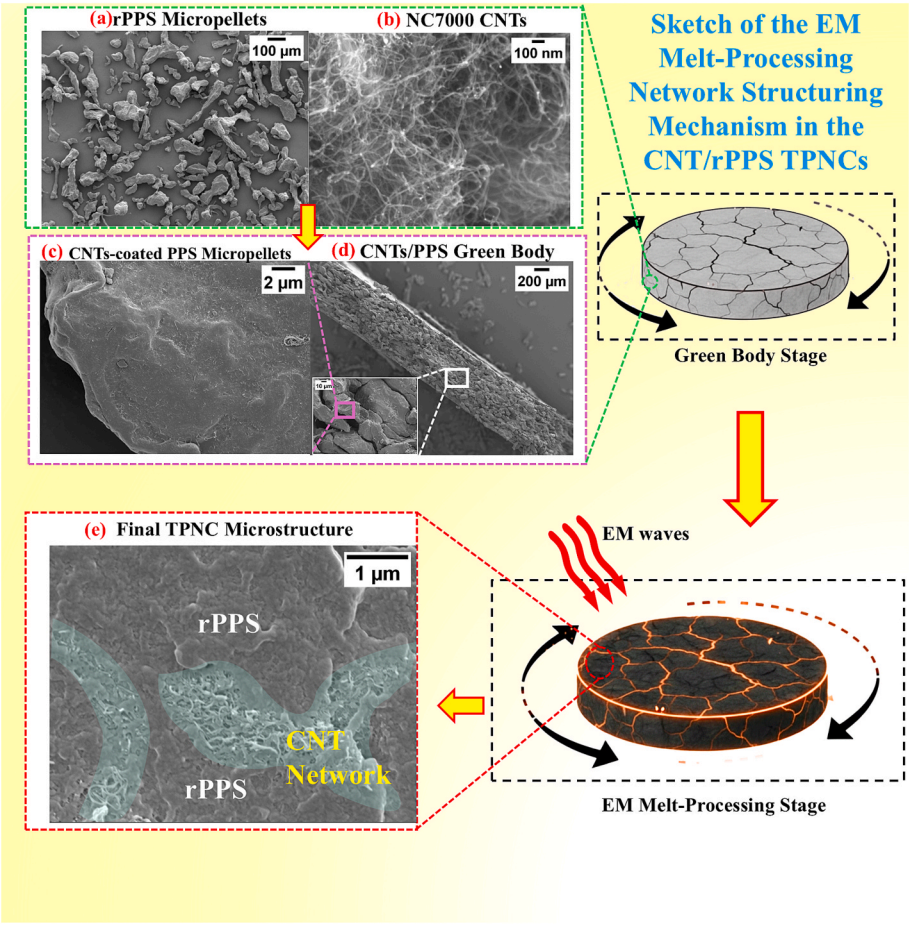

Fig. 1. Schematic representation of the network structuring mechanism (network formation) that takes place in the TPNCs via EM melt-processing. Inserted SEM micrographs of (a) rPPS micropellets, (b) pristine NC7000 CNTs, (c) CNT-coated rPPS micropellets, (d) cross-section of the GB, and (e) microstructure of the resulting segregated networks in the TPNCs upon irradiation.

Fig. 1a shows the rPPS micropellets before mixing. The micropellets display irregular shapes with relatively smooth surfaces, reflecting the typical features of mechanically recycled semiductile polymeric material. Fig. 1b shows the morphology of the pristine NC7000 CNTs, which exhibit a highly entangled, web-like nanotube network. Fig. 1c displays the surface of the rPPS micropellets after mixing, which becomes uniformly covered by CNTs, yielding fully CNT-coated rPPS micropellets. Such a level of coating is a key prerequisite for forming an interconnected CNT network that, once in the GBs and TPNCs, will lead to segregated conductive architectures, as reported in our earlier work [17,32]. It can be observed that the CNTs adhere strongly to the polymer surface, forming continuous CNT percolated pathways between adjacent micropellets in the GBs, as seen in Fig. 1c and 1d.

Upon mechanical compaction, the CNT-coated rPPS micropellets undergo densification, bringing the CNT-coated surfaces into close contact in the GB (Fig. 1d). The resulting inter-pellet junctions facilitate the establishment of an interconnected CNT network throughout the compacted GB. The interphase region between the rPPS micropellets, which contains the CNT-rich zones in Fig. 1d, highlights the presence of tightly packed CNT bundles bridging the rPPS micropellets' boundaries. This morphological evidence indicates that the preformed segregated topology is preserved after compaction, ensuring efficient percolation and electron transport across the whole GB.

As depicted in Fig. 1e, upon EM melt-processing, distinct structural transformations occur. The partial deformation and coalescence of the rPPS micropellets lead to the formation of dense polymer domains separated by the CNT-enriched interfaces that form the network, but also to a partial distortion of the CNT network. This confirms the successful creation of a segregated but percolated microstructure, characterized by localized CNT networks outlining the polymer boundaries, an arrangement known to yield high electrical conductivity and better EMI SE [33]. Nevertheless, the retention of the CNT-rich interphase and interfacial regions after the EM irradiation step demonstrates that localized interfacial heating enabled melting of rPPS micropellets at contact points without the dull disruption of the macro-scale network continuity.

As highlighted in Fig. 1e, CNTs are found embedded within the rPPS micropellets themselves. During EM irradiation, the CNT network absorbs microwave energy, generating localized hotspots that initiate rPPS melting and flow. This controlled interfacial and bulk melting promotes interpenetration and wetting of polymer chains onto CNT bundles, resulting in strong polymer-CNT interfacial adhesion. However, limited CNT diffusion into the polymer matrix is also observed, suggesting slight relaxation of the originally sharp interface. While such redistribution may slightly reduce the degree of network segregation, it contributes to improved mechanical interlocking and stress transfer across CNT-polymer interfaces, balancing electrical performance with structural integrity. The SEM observations in Fig. 1 provide direct morphological evidence for the formation and partial retention of CNT-rich interfacial regions before and after EM melt-processing, supporting the proposed interfacial consolidation mechanism.

Overall, the microstructural observations confirm that the EM melt-processing route effectively transforms CNT-coated rPPS micropellets into a densely fused "monolithic" nanocomposite structure with a well-segregated but percolated microarchitecture, a combination difficult to achieve by conventional polymer processing methods. The hierarchical multiscale structure thus attained, comprising CNT-rich networks surrounding rPPS micropellets, is central to the enhanced electrical conductivity and EMI SE discussed in subsequent sections.

Electrical conductivity and percolation

Fig. 2 and Table 1 display the variation in volume electrical conductivity (σ) with CNT loading in both GBs and EM-processed TPNCs. Conductivity measurements show that segregated structures by EM melt-processing significantly enhance conductivity with minimal nanoparticle addition, outperforming the typical randomly dispersed networks in conventionally (i.e., melt-mixing) processed nanocomposites. The observed sharp upturn in conductivity as the CNT loading surpasses the percolation threshold (ϕ_c) conforms (at least in

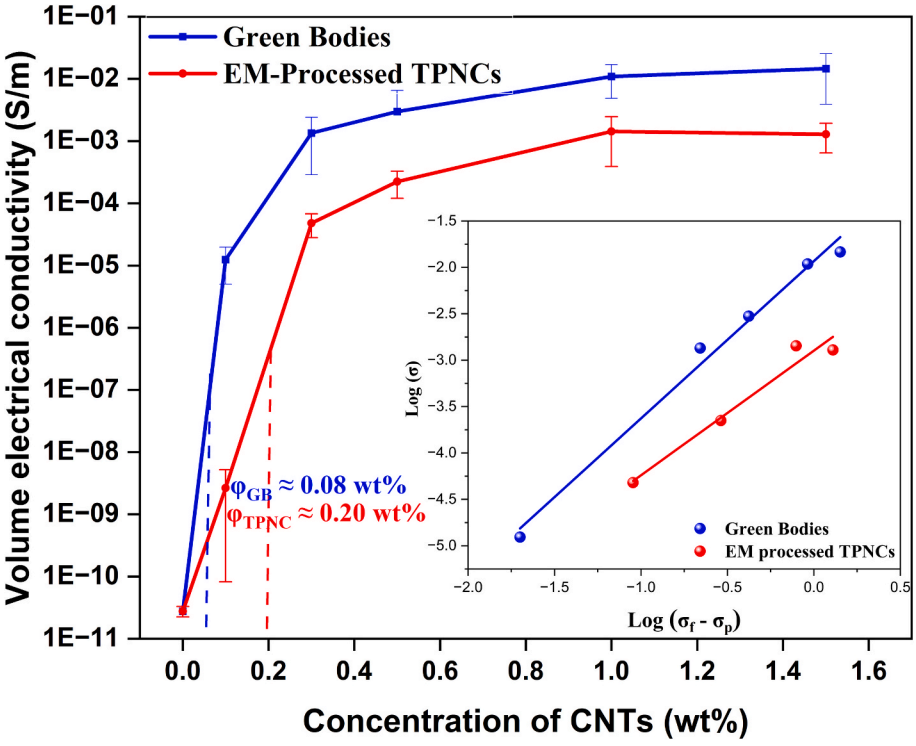

Fig. 2. Through-thickness volume electrical conductivity of GBs and their respective EM-processed TPNCs at corresponding CNT loadings. Error bars represent 95% confidence intervals. The inset displays the calculations for the percolative parameters.

Table 1
Average through-thickness volume electrical conductivity of pristine rPPS, CNT/rPPS GBs, and EM-processed TPNCs measured using disc-shaped specimens at different CNT loadings. Values represent the average conductivity for each CNT loading, with variability reported as 95% confidence intervals.

Formulation	Green Bodies (S/m)	EM-processed TPNCs (S/m)
rPPS	$(2.76 \pm 0.52) \times 10^{-11}$	$(2.76 \pm 0.52) \times 10^{-11}$
0.1% CNT/rPPS	$(1.24 \pm 0.74) \times 10^{-5}$	$(2.64 \pm 2.56) \times 10^{-9}$
0.3% CNT/ rPPS	(1.35 ± 1.06) × 10–3	$(4.80 \pm 1.98) \times 10^{-5}$
0.5% CNT/ rPPS	(2.98 ± 3.56) × 10–3	$(2.24 \pm 1.04) \times 10^{-4}$
1.0% CNT/ rPPS	(1.09 ± 0.60) × 10–2	$(1.43 \pm 1.00) \times 10^{-3}$
1.5% CNT/ rPPS	(1.47 ± 1.08) × 10–2	$(1.29 \pm 0.64) \times 10^{-3}$

general) to established percolation theory, described by equation (6) [34]:

$$\sigma = \sigma_0(\phi - \phi_c)^t \tag{6}$$

Where σ is the electrical conductivity at a given CNT volume fraction (ϕ), σ_0 is a fitting constant typically associated with the plateau conductivity of fully percolated composites, and t is the critical exponent describing the scaling behavior of the conductive network [17,35].

As seen in Fig. 2, the GBs achieved up to six orders of magnitude enhancement in conductivity from $(2.76 \pm 0.52) \times 10^{-11}$ S·m^{-1} for neat rPPS up to $(1.24 \pm 0.74) \times 10^{-5}$ S·m^{-1} at only 0.1 wt% CNT, with the EM-processed TPNCs following closely. Despite minor reductions in conductivity attributed to the partial network relaxation during the EM melt-processing of TPNCs, the conductive thresholds remain significantly lower than those from conventional melt-mixed CNT/rPPS TPNC systems (2–3 wt%) [36], underscoring the potential of the proposed EM melt-processing for raising transport properties in HP polymers. Importantly, these enhancements are achieved while preserving the recyclability and eco-efficiency inherent to rPPS.

In percolation theory, t values of approximately 1.3 and 2.0 are associated with two-dimensional and three-dimensional conductive networks, respectively [16]. However, in CNT-based polymer nanocomposites, experimentally reported t values span a broad range (1.3——4.0) due to their complex, non-ideal nature of charge transport, including tunneling-dominated conduction [37,38], nanoparticle aggregation, interfacial confinement, and polymer-particle interactions [39]. It is therefore generally accepted that $t > 2$ reflects predominantly three-dimensional (3D) bulk conductive networks, whereas $t < 2$ is characteristic of two-dimensional (2D) or quasi-two-dimensional conductive networks formed within confined or interfacial domains of polymer nanocomposites [16,40]. Nevertheless, Park et al. state that, when the critical exponent t is between 1.1 and 1.3, the percolated network is regarded as 2D percolation, whereas when t is in the range 1.6 to 2.0, as 3D percolation [41].

In our research, the extracted critical exponent for the GB specimen set is $t \approx 1.63$, while the EM-processed TPNCs exhibit a lower value of $t \approx 1.33$. Both values are below 2, indicating that charge transport is dominated by interfacially confined CNT networks rather than isotropic bulk percolation. The slightly higher t for the GBs is consistent with a denser and more rigid segregated CNT shell localized at pellet-pellet boundaries, where a highly constrained, contact-rich network produces a steeper conductivity increase above ϕ_c [39]. In contrast, the lower t observed for the EM–processed TPNCs suggests a more quasi–2D interfacial network, in which EM melt–processing partially redistributes CNTs and slightly relaxes the continuity of the segregated shell while still maintaining efficient charge transport via tunneling across short interparticle gaps along the CNT-coated polymer micropellets' interfaces [27,37,41].

As expected, the electrical percolation threshold of the TPNCs is substantially reduced by the formation of segregated network structures. Thus, based on Fig. 2, at an ultralow CNT loading of approximately 0.08 wt%, the GB specimens percolate, whereas the EM-processed TPNCs exhibit a somewhat higher threshold of about 0.20 wt%, corresponding to a 2.5-fold increase factor relative to the GBs, yet remaining well below the values typically reported for rPPS-based CNT nanocomposites [36,42].

In both GB and TPNC states, SEM (Fig. 1) reveals CNTs tightly packed along the rPPS pellet boundaries, forming highly interconnected charge transport pathways. For the GBs, the undisturbed segregated network supports a higher initial conductivity, while EM melt-processing slightly redistributes the CNTs through localized melting, merely relaxing the network but maintaining effective interfacial conduction routes and mechanical interlocking [32]. Thus, both architectures efficiently convert polymer micropellets and nanoparticles into segregated configurations that foster continuous electron conduction at ultralow CNT loadings.

Charge transport below and near ϕ_c is dominated by quantum tunneling and phonon-assisted hopping, owing to nanometric intergranular CNT distances [43]. Thermal excitation further facilitates tunneling, while minor CNT migration into rPPS in EM-processed samples enhances mechanical stability without significantly impeding percolation [43]. Beyond the percolation threshold, conductivity quickly saturates, reflecting the onset of metallic-like transport and fully connected CNT networks [35]. In this regime, conductivity plateaus indicate the establishment of robust and extended conduction pathways, a direct consequence of the engineered segregated microstructure.

In summary, both GBs and TPNCs use engineered segregated CNT networks to achieve strong conductivity gains and robust percolation at ultralow CNT loadings in recycled PPS. These results demonstrate that tailored CNT network structuring and EM melt-processing enable the formation of electrically conductive pathways in CNT/rPPS nanocomposites at low CNT loadings, as reflected by the enhanced through-thickness electrical conductivity.

Electromagnetic Interference Shielding Effectiveness (EMI SE).

Fig. 3 presents the EMI SE (X-band), its components, and power coefficients for the GBs and EM-processed TPNCs as a function of CNT content. Notably, at a CNT loading of only 1.5 wt%, the GBs exhibit a total EMI SE of 6.27 dB at 8.2 GHz, while the EM-processed TPNCs reach 2.97 dB. Although these absolute values are moderate compared to those of heavily loaded systems, they are achieved at CNT loading levels orders of magnitude lower and with sub-millimeter thicknesses (~0.6–0.8 mm), underscoring the efficiency of the segregated CNT architectures. This also demonstrates the residual EM susceptibility of the materials.

As evident from Fig. 3b and 3c, the absorptive (EMI SE_A) and reflective (EMI SE_R) shielding components increase with CNT loading in both GBs and TPNCs. EMI SE_A becomes the dominant mechanism at higher concentrations, which correlates well with the observed increase in electrical conductivity. Specifically, in both GBs and TPNCs at 1.5 wt % CNT, EMI SE_A contributes approximately 70–80% of the total EMI SE, while EMI SE_R remains comparatively low and increases only modestly with CNT concentration. For instance, in the GBs, EMI SE_A increases from ~ 0.5 dB at 0.1 wt% to ~ 4.5 dB at 1.5 wt%, whereas EMI SE_R increases only from ~ 0.2 to ~ 1.5 dB over the same concentration range. A similar trend is observed for the EM-processed TPNCs, where EMI SE_A consistently exceeds EMI SE_R despite the overall lower EMI SE. The dominance of EMI SE_A is fully consistent with segregated conductive network architectures, in which CNTs are concentrated along pellet-pellet interfaces and interparticle junctions, forcing incident waves to repeatedly penetrate and traverse CNT-rich interfacial regions [44]. Within these regions, electromagnetic energy is dissipated via ohmic losses in the percolated CNT network, interfacial polarization at CNT/rPPS boundaries, and multiple internal reflections between adjacent CNT-coated micropellets or microdomains [45,46]. Similar absorption-dominant behavior has been widely reported for segregated CNT/polymer systems, such as CNT/ polylactic acid (PLA) [47], CNT/ ultra-high molecular weight polyethylene (UHMWPE) [48], and PPS/ graphene nanoplatelet (GNP) composites [49], where micro–interface

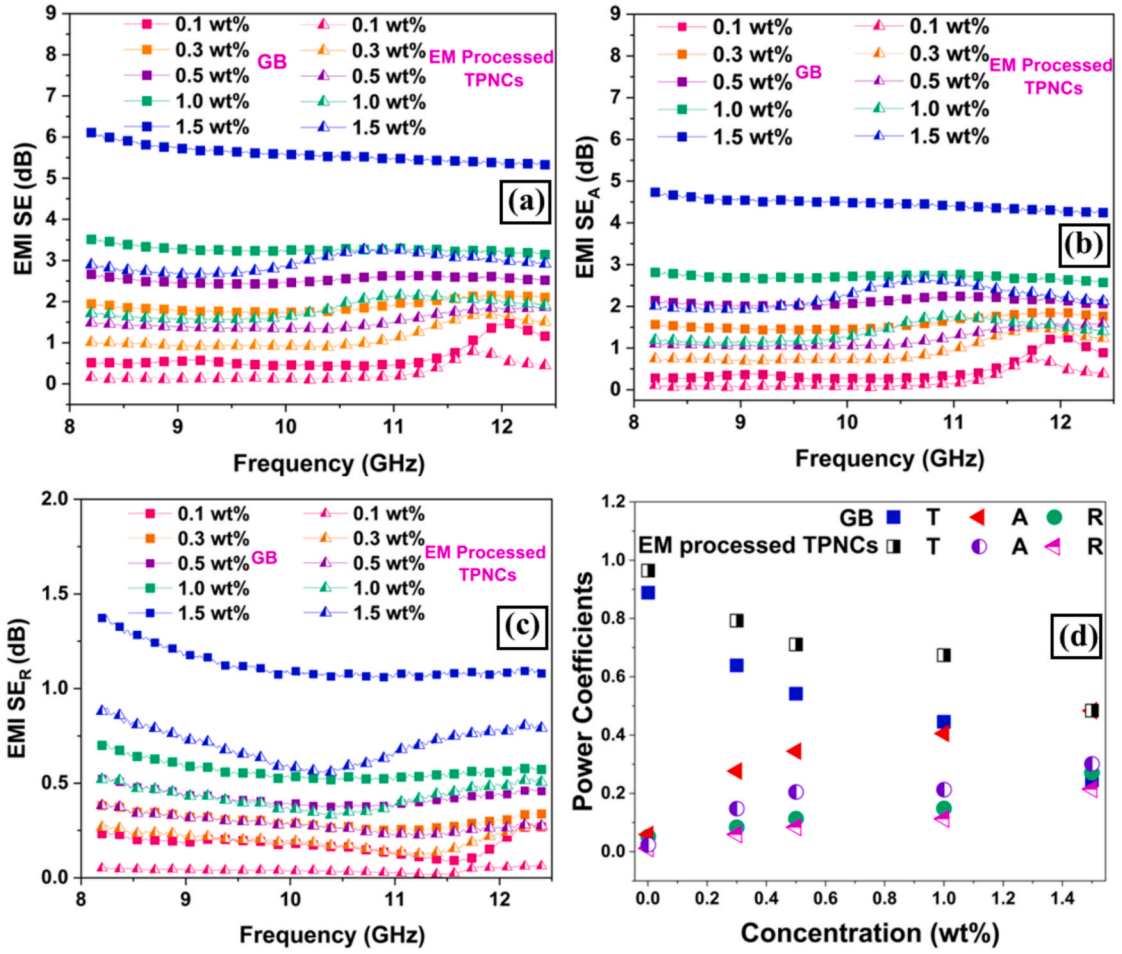

Fig. 3. (a) Representative EMI SE as a function of frequency (X-band) for the GBs and EM-processed TPNCs at various CNT contents. EMI SE (b) absorption (EMI SE_A) and (c) reflection (EMI SE_R) components for GBs and EM-processed TPNCs, respectively. (d) Comparison of T, R, and A power coefficients as functions of concentration at 8.2 GHz.

confinement of conductive fillers markedly enhances wave attenuation efficiency at low nanoparticle loadings, in contrast to randomly dispersed melt–blended CNT/PPS [36], which typically demands much higher CNT contents to reach comparable EMI SE. In such composite systems, thick sections and heavy loadings (~15 wt% CNT) are often required to approach total EMI SE values that segregated architectures can attain with a fraction of the particles and thickness, highlighting the superior conductive particle utilization and absorption efficiency of segregated networks for this purpose [36,50].

A direct comparison of GBs and EM-processed TPNCs highlights the crucial role of mesoscale morphology in determining EMI SE performance. GBs consistently display a higher total EMI SE than their EM-processed samples at the same CNT loading, which is attributed to a surface-localized particle microstructure that concentrates CNTs along particle boundaries, interstitial regions, and roughened interfaces generated by ball milling. This topology maximizes both the number of conductive junctions and the effective interfacial area available for wave-matter interactions, closely resembling the segregated network systems, where interfacial CNT confinement yields ultralow percolation thresholds, and absorption-dominated shielding at comparatively low loadings [47,51]. In contrast, EM melt–processing densifies the bulk, improves polymer-CNT interfacial adhesion, and partially relaxes the sharp segregated shell by redistributing some CNTs into the interior rPPS domains [52]. As shown in the SEM micrographs of Fig. 1e, due to the high melt temperature reaching above the melting point of PPS during irradiation, there is a migration of CNTs into the low-viscosity matrix, which distorts the initially structured CNT conductive pathways in TPNCs. This morphological relaxation smooths interparticle contacts, reduces micro-scale roughness, and diminishes the exposure of CNT-rich regions directly to the incident field, thereby lowering the density of scattering centers and internal reflection pathways [47]. Consequently, the EMI SE_A and total EMI SE components decrease even though the electrical conductivity remains high, a trend consistent with prior observations that transforming highly confined, segregated, or interfacial-localized networks into more homogeneous morphologies weakens dominant absorption by reducing opportunities for multiple scattering, ohmic dissipation, and dielectric polarization within the nanocomposite [28]. Moreover, EMI SE in conductive polymer composites arises from the combined contributions of the power coefficients: T, R, and A. Fig. 3d summarizes the evolution of the power coefficients as a function of CNT concentration at 8.2 GHz for both GBs and EM-processed TPNCs. Across all CNT loadings, T decreases monotonically with increasing CNT content for both material systems, indicating progressively enhanced attenuation of incident electromagnetic waves. Notably, GBs exhibit consistently lower transmission than their EM-processed TPNCs at equivalent CNT loadings, reflecting the more continuous and surface-localized CNT networks present in the GBs. These dense interfacial networks increase electrical conductivity and reduce electromagnetic penetration depth, thereby suppressing wave transmission even at ultralow CNT contents. On the other hand, R shows a gradual increase with CNT concentration in both systems, consistent with the rise in electrical conductivity and the resulting impedance mismatch at the air-composite interface. However, the magnitude of R remains substantially lower than that of A across the entire CNT loading

range. This indicates that reflection plays a secondary role in the shielding of these systems, even as conductivity increases. The relatively modest reflection contribution suggests that the TPNCs avoid excessive surface impedance mismatch, which is advantageous for minimizing secondary electromagnetic pollution [28].

Mechanical properties of TPNCs

The average values of Young's modulus, tensile strength, and elongation-at-break obtained from tensile testing for the different TPNCs are shown in Fig. 4, along with their respective 95% confidence interval error bars. A summary of the average tensile data and their variability for the EM-processed TPNCs is also presented in Table 2. The inclusion of CNTs notably influences the stiffness and strength of the rPPS matrix; however, the effect varies with CNT loading due to competing mechanisms of CNT–induced load transfer and network reinforcement versus CNT agglomeration, stress concentration, micro-void formation, and constrained polymer chain mobility [53,54].

At low CNT loadings, specifically at 0.1 wt%, as shown in Fig. 4a, the TPNCs show the greatest and most remarkable mechanical improvement. Here, tensile strength increases to 80.77 ± 8.22 MPa, which is ~ 72% significantly higher than that of rPPS at 46.78 ± 3.77 MPa. Likewise, the modulus (Fig. 4b) reaches 3.537 ± 0.479 GPa, meaning a ~ 99% increase over the neat rPPS (1781.5 ± 479.3 MPa). Moreover, at 0.1 wt%, the elongation-at-break (Fig. 4c) of the TPNCs is quite preserved, 4.14 ± 0.67%, showing no statistically significant difference when compared to rPPS (3.31 ± 0.31%). These gains are attributed to the strategic localization of CNTs along rPPS microdomain boundaries in the segregated network architecture, resulting in efficient stress transfer and chain alignment under load effects, supported by recent studies showing up to a 65% increase in tensile strength for uniformly dispersed CNT nanocomposites at similar low loadings [53,55]. These concurrent gains in strength and stiffness at low CNT loading suggest improved interfacial stress transfer, likely enabled by the segregated CNT network and proposed processing method [53]. In fact, the CNTs within the EM-structured network act as bridges between neighboring rPPS domains, restricting localized plastic deformation and inducing alignment of polymer chains during tensile loading [56]. This advanced load transfer is consistent with micromechanical models for nanocomposite reinforcement, which attribute enhanced modulus and strength to homogeneous filler distribution, increased interface area, and strong matrix-filler interactions [57].

Table 2
Average tensile testing results for the EM-processed TPNCs and the rPPS matrix.

Formulation	Modulus (GPa)	Tensile Strength (MPa)	Elongation-at-break (%)
rPPS	1.781 ± 0.479	46.79 ± 9.77	3.31 ± 2.02
0.1% CNT/ rPPS	3.537 ± 0.479	80.77 ± 8.22	4.14 ± 0.68
0.3% CNT/ rPPS	2.700 ± 0.633	52.82 ± 7.81	2.91 ± 0.76
0.5% CNT/ rPPS	2.589 ± 0.252	50.89 ± 5.59	3.19 ± 0.39
1.0% CNT/ rPPS	2.021 ± 0.235	44.79 ± 4.35	3.78 ± 0.36
1.5% CNT/ rPPS	2.712 ± 0.252	55.50 ± 7.51	3.36 ± 0.81

At higher CNT loadings (≥ 0.3 wt%), the tensile strength, elongation-at-break, and modulus show a sharp decrease. This decline may be attributed to increased CNT agglomeration and weaker interfacial adhesion between CNT clusters and the rPPS matrix. In the segregated architecture formed by ball-milling and EM processing, CNTs are concentrated at inter-domain boundaries, whose excessive localization and accumulation can generate micro-voids and stress concentrations

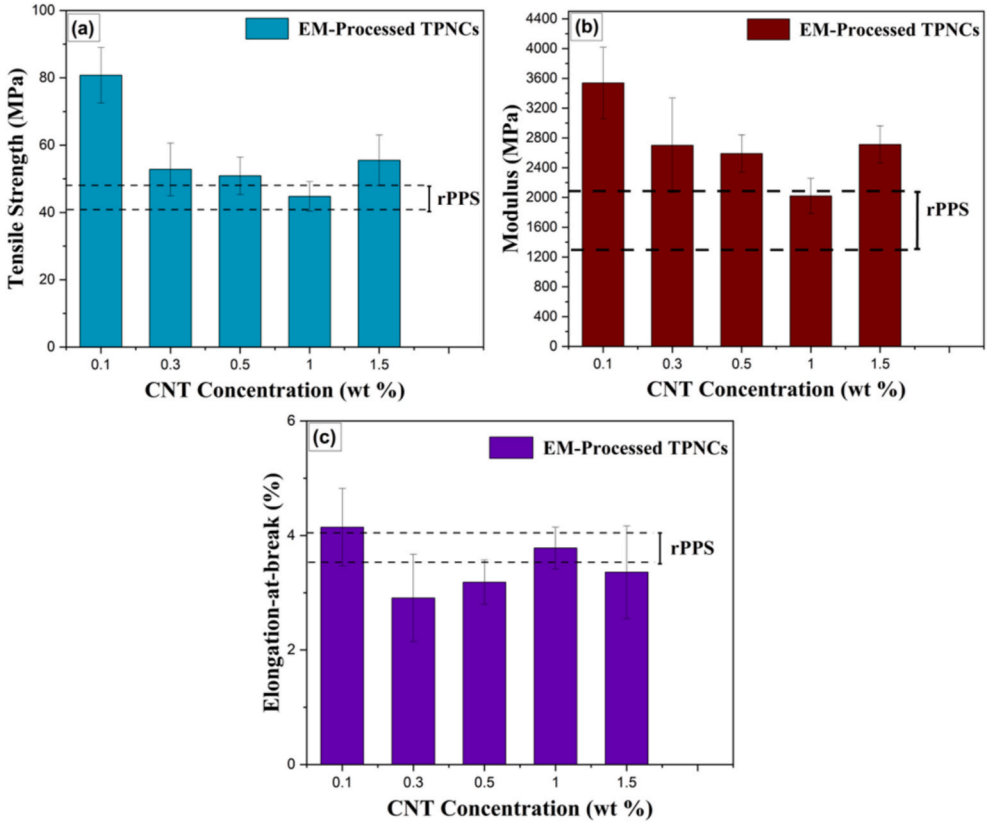

Fig. 4. Tensile mechanical properties of the TPNCs as functions of CNT concentration (wt.%). (a) tensile strength, (b) modulus, and (c) elongation-at-break. The dotted lines represent rPPS matrix properties, and the error bars are 95% confidence intervals.

due to high-temperature hot-spots, degrading the matrix and its mechanical performance [32]. Similar mechanical softening at higher loadings has been reported in other CNT-filled thermoplastic systems, where non-uniform dispersion and filler-induced defects reduce load-bearing capacity [58,59].

The non-linear mechanical response is further supported by the representative SEM images provided in Fig. S2, which shows the EM-processed TPNC morphologies at high CNT loadings. These images indicate that the segregated CNT-rich interfacial network is generally retained after EM melt-processing; however, the morphology becomes increasingly heterogeneous as CNT content increases. At low CNT loading (Fig. 1), the CNT-rich interfaces appear more uniformly distributed along the fused rPPS microdomain boundaries, which can promote interdomain stress transfer and mechanical interlocking. In contrast, at higher CNT loadings, the CNT-rich boundary regions become more crowded, increasing the likelihood of local CNT accumulation, partial network distortion, micro-void formation, and stress-concentration sites. Therefore, the tensile response is governed by a balance between CNT-mediated interfacial reinforcement and morphology-induced defects, rather than by a simple linear dependence on CNT loading.

Overall, these results suggest that low CNT loading, particularly $<$ 0.3 wt%, provides the most favorable balance of stiffness, strength, and retained ductility in the EM-processed TPNCs. The mechanical response does not increase linearly with CNT content because the beneficial effects of CNT-mediated interfacial reinforcement are progressively counterbalanced by CNT accumulation, heterogeneous redistribution, and stress-concentration effects at higher loadings. These findings highlight the importance of optimizing CNT concentration and EM-processing conditions to preserve the segregated conductive architecture while maintaining mechanical integrity.

Rheological results

a) Time-dependent response.

Fig. 5 and Fig. S3 displays the time-dependent viscosity, $\eta^{+}(t) = \tau(t)/\dot{\gamma}$, after start-up of steady shearing of the materials at 3 different shear rates (stress-growth test). Neat rPPS shows a mild shear-thinning behavior and limited melt elasticity, demonstrated by a moderate stress overshoot, confirming the absence of microstructural mechanisms for significant stress build-up. Nevertheless, the presence of CNTs dramatically alters this behavior in the GBs and TPNCs. As shown in Fig. 5a, for 0.1 wt% CNT, both GB and EM melt-processed TPNCs exhibit significantly increased viscosities with respect to rPPS, likely due to polymer chain adsorption onto CNT surfaces and the CNT network effect [60]. This chain adsorption increases the effective hydrodynamic volume surrounding each CNT in the network and restricts local chain mobility, resulting in significantly higher viscous drag than in composites containing microparticles [61]. As a result, even at ultralow CNT loadings, both GBs and EM-processed TPNCs show a remarkable increase in melt viscosity relative to neat rPPS. The magnitude and shear-rate dependence of this increment, however, strongly depend on CNT network connectivity and mobility, both of which are dictated by the processing route [61,62]. At 0.1 wt% CNTs, the EM-processed TPNCs show shear-thinning behavior with some late-time thickening. The same shear thinning behavior is less pronounced in the neat rPPS and GBs.

Although the EM-processed TPNCs begin with a higher initial viscosity, reflecting early-stage CNT connectivity enabled by microwave-induced interfacial melting, the network remains above the electrical percolation, but below the rheological percolation threshold. Consequently, CNTs are only weakly interconnected, and the network lacks the structural integrity required to undergo flow-induced densification [63]. The slight late-time thickening observed in the GBs and TPNCs does not constitute a true shear thickening behavior but instead reflects slow network stabilization, where CNTs gradually relax, align, and increase local connectivity without forming a dense, load-bearing microstructure, and even some polymer crosslinking effects. This behavior is characteristic of weakly percolated CNT systems where the CNT loading is insufficient for significant stress-induced restructuring [64].

At higher CNT loading (i.e., above 0.3 wt%), the rheological responses become remarkably different across the GBs and the EM melt-processed TPNCs. As shown in Fig. 5b, the EM-processed TPNCs display a distinctive stress overshoot or upturn behavior, particularly at $\dot{\gamma} = 1.0\ s^{-1}$, in which $\eta^{+}(t)$ initially decreases, consistent with early network breakage, followed by a growth in viscosity as shear continues. This viscosity reduction is a behavior in segregated CNT systems and arises from the weakening of the interfacial CNT network during EM melt-processing. In fact, at higher CNT concentrations, the microwave field generates more intense, localized heating at CNT-rich boundaries, causing deeper rPPS penetration into CNT shells and partial redistribution of CNTs into the polymer domains [32]. This redistributes and dilutes the segregated CNT layer, reducing network continuity and lowering the effective CNT-CNT contact density [65]. Additionally, higher CNT loading promotes re-agglomeration during ball milling and EM-susceptibility, likely decreasing the effective aspect ratio and reducing the nanofiller surface available for polymer adsorption. Both effects, network dilution and CNT agglomeration, decrease the effective hydrodynamic volume of the connected CNT network and the amount of polymer dynamically coupled to it, thereby reducing melt resistance and ultimately lowering viscosity [60]. This phenomenon is indicative of shear–induced network reconstruction, where CNTs disrupted by the initial flow reapproach, align, and form new contact junctions driven by hydrodynamic forcing, as observed in studies of CNT/polymer melts and CNT assemblies subjected to shear, which report flow-induced network breakdown followed by post–flow reconnection and rearrangement of

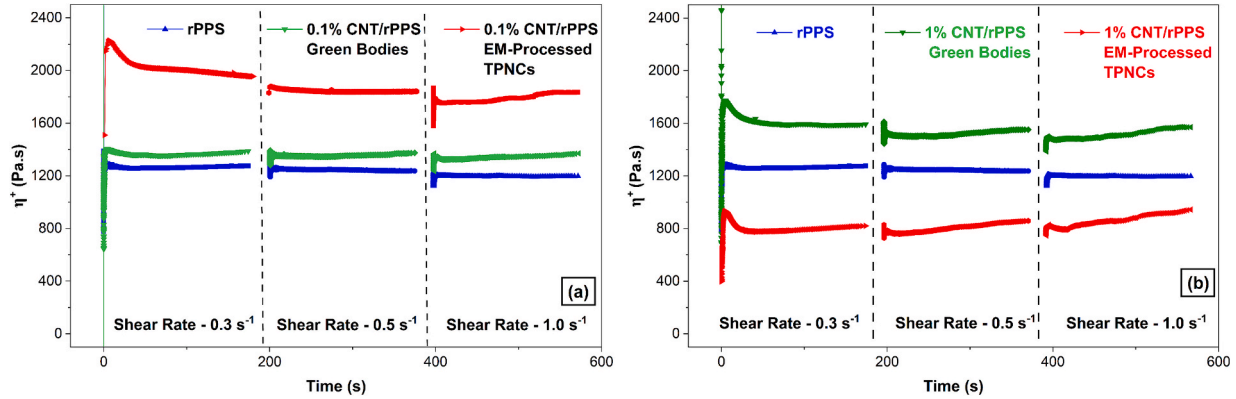

Fig. 5. Transient shear viscosity (η^{+}) at 320 °C for the rPPS, GBs, and EM processed TPNCs at (a) 0.1 wt% CNT, and (b) 1 wt% CNTs.

CNT bundles [66]. Specifically, it indicates shear-induced formation of percolated clusters spanning the system above a critical shear rate [65]. Microwave processing plays a key role: it melts CNT-coated rPPS pellets selectively at CNT-rich interfaces, allowing CNTs to remain sufficiently mobile and enabling reconstruction under shear while preserving long CNT structures that can re-entangle. Consequently, EM-processed materials support both network breakage and network re-formation, a prerequisite for overshoot or thickening-like responses [65]. As shown in Fig. 5b, GBs at 1 wt% exhibit a shear thinning behavior with a higher stress overshoot, as their segregated CNT shells remain rigidly confined to rPPS particle boundaries, restricting CNT mobility, and preventing CNT re-agglomeration [67]. While CNTs reorganize locally under flow (alignment), this limited mobility prevents network reconstruction; viscosity thus decreases monotonically as shear disrupts the pre-existing loose network [61]. In contrast, Fig. 5 shows that EM-processed TPNCs at 1 wt% exhibit a remarkably lower viscosity than both rPPS and the corresponding GBs across all shear rates, indicating a very substantial reduction in melt resistance after electromagnetic melt-processing. This decrease is consistent with microwave-induced restructuring and partial dilution of the segregated CNT network, which weakens the load-bearing interfacial shell and facilitates flow [60]. At the same time, microwave heating of CNT-rich regions is known to generate localized thermal hotspots that can, under certain conditions, promote chain scission or oxidative degradation in thermoplastics, leading to a further drop in melt viscosity, via chain scission and breakdown that reduces molecular weight [68]. Thus, while rheology clearly evidences a softened, less resistant melt after EM melt-processing, the plotted response alone cannot distinguish between pure microstructural modification and a partial reduction in matrix molecular weight, and additional molecular–weight or chemical analyses would be required to confirm the extent of degradation.

b) Dynamic response.

Dynamic oscillatory time-sweep measurements, displayed in Fig. 6, were performed at a representative CNT loading of 0.5 wt% to compare the rheological response and network evolution of pristine rPPS, the CNT/rPPS GB, and the EM-processed TPNC under identical testing conditions. It further confirms the network evolution inferred from steady-shear measurements. Both storage (G′) and loss (G″) moduli increase sharply with CNT inclusion, consistent with strong rPPS-CNT interfacial adsorption and the development of CNT-mediated elasticity [62]. The EM-processed TPNCs reach the G′-G″ crossover ("pseudo-gel point") earlier than both GBs and rPPS, reflecting a rapidly forming physical network of CNT entanglements, CNT-CNT contacts, and crystallization-assisted rPPS elasticity. The observed G'/G" crossover is consistent with the formation of a strongly connected network within the CNT/rPPS melt, which could originate either from EM–processing-induced chemical crosslinking or from physical gelation and/or crystallization of the segregated TPNC microstructure [66,69]. However, additional targeted experiments (e.g., multi-frequency gel–point analysis, thermo–reversibility studies, and complementary chemical/thermal characterization) are required to discriminate unambiguously between chemical crosslinking and purely physical network formation [69].

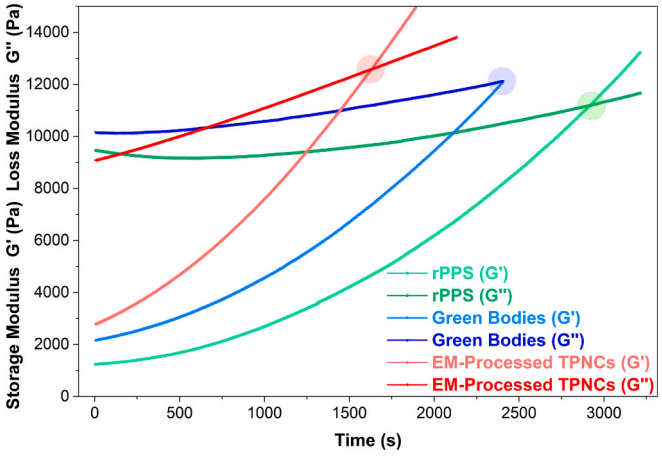

Fig. 6. Time-sweep dynamic shear analysis comparing pristine rPPS, 0.5 wt% CNT/rPPS GB, and 0.5 wt% CNT/rPPS EM-processed TPNC at 1% strain, 1 Hz, and 320 °C.

The rheological response of the TPNC melts exhibits a clear correspondence with the trends in bulk mechanical properties across the investigated CNT loadings. At low CNT content (0.1 wt%), the increases in complex viscosity and storage modulus indicate the formation of a more effectively load-bearing microstructure, consistent with the concurrent enhancements in tensile strength and modulus observed for EM-processed TPNCs [70]. At higher CNT contents, the onset of CNT agglomeration and reduced mobility of the CNT network is reflected in a diminished rheological reinforcement, which parallels the deterioration or plateauing of mechanical performance [71].

Conclusion

In this study, we demonstrated a potential and effective pathway for upcycling recycled PPS into high-performance, multifunctional TPNCs using our innovative EM melt-processing approach. By combining solid-state ball milling with rapid, selective EM heating, we achieved controlled localization of multi-walled CNTs within a segregated composite microstructure that enabled ultralow electrical percolation thresholds, EM-susceptibility, and enhanced functional performance.

SEM imaging confirmed the formation of CNT-rich interfacial networks in the GBs and their partial reconstruction after EM melting, resulting in hierarchical conductive architectures that retained long-range connectivity at extremely low filler contents. Thus, the electrical conductivity measurements of such GBs revealed a dramatic enhancement of six orders of magnitude at only 0.1 wt% CNT, highlighting the efficiency of the segregated network in enabling charge transport through both tunneling and percolative conduction. Correspondingly, the TPNCs exhibited absorption-dominated EMI shielding, an indirect measure of EM-susceptibility, achieving competitive shielding values at only 1.5 wt% CNT and sub-millimeter thicknesses. Mechanical testing further demonstrated that very low CNT loadings (0.1 wt% or 0.06 vol %) significantly improved tensile stiffness and strength, validating effective stress transfer across the CNT-rPPS interphase while emphasizing the importance of avoiding excess filler that compromises mechanical integrity through agglomeration and interfacial defects. This is significant from the upcycling perspective.

Rheological analysis provided deep insight into CNT network dynamics under melt conditions. EM-processed TPNCs displayed distinctive viscoelastic behavior: early pseudo-gelation and, at higher loadings, late-time thickening behavior, likely arising from the mobility and reconstruction of partially segregated CNT networks during shear deformation. The correlation between rheology, mechanical performance, and electrical behavior confirms that EM melt-processing not only preserves CNT aspect ratio and network mobility but also enables dynamic reorganization of the CNT network architecture, a phenomenon rarely observed in conventionally melt-mixed nanocomposites.

Overall, this work establishes EM melt-processing as a promising and energy-efficient route for converting highly crystalline, difficult-to-process recycled PPS into advanced HP TPNCs with tunable electrical, electromagnetic, mechanical, and rheological properties. The strategy enables simultaneous improvements in processability, microstructural control, and multifunctionality at extremely low filler contents, offering a scalable platform for sustainable HP materials and advanced manufacturing. These findings open new avenues for integrating recycled PPS into lightweight structural components, electromagnetic

compatibility enclosures, and next-generation electrical and thermal management systems across the automotive, aerospace, space, and energy sectors.

CRediT authorship contribution statement

Madara Mohoppu: Writing – original draft, Visualization, Validation, Methodology, Investigation, Formal analysis, Data curation, Conceptualization. **Utsab Ayan:** Writing – review & editing. **Bibek Kattel:** Writing – review & editing, Investigation. **Oussama Oulhakem:** Writing – review & editing, Investigation. **Olivia McNair:** Resources. **Ahmed Al-Ostaz:** Resources, Funding acquisition. **Enrique Jackson:** Writing – review & editing, Funding acquisition. **Byron S. Villacorta:** Writing – review & editing, Writing – original draft, Validation, Supervision, Resources, Project administration, Methodology, Investigation, Funding acquisition, Formal analysis, Conceptualization.

Declaration of competing interest

The authors declare that they have no known competing financial interests or personal relationships that could have appeared to influence the work reported in this paper.

Acknowledgment

This work was supported by a National Aeronautics and Space Administration (NASA) cooperative Agreement [Award No. 80NSSCM0041].

Disclaimer Statement: "The material contained in this document is based upon work supported by a National Aeronautics and Space Administration (NASA) cooperative agreement. Any opinions, findings, conclusions, or recommendations expressed in this material are those of the author and do not necessarily reflect the views of NASA."

Also, Kenneth Hulugalla (PhD candidate, Department of Biomolecular Sciences, University of Mississippi, USA) is kindly thanked for providing access to the BioRender software.

Appendix A. Supplementary data

Supplementary data to this article can be found online at https://doi.org/10.1016/j.compositesa.2026.110041.

Data availability

Data will be made available on request.

References

[1] Montagna LS, Kondo MY, Callisaya ES, Mello C, de Souza BR, Lemes AP, et al. A review on research, application, processing, and recycling of PPS based materials. Polimeros 2022;32. https://doi.org/10.1590/0104-1428.20210108.

[2] Chen G, Mohanty AK, Misra M. Progress in research and applications of Polyphenylene Sulfide blends and composites with carbons. Compos B Eng 2021; 209:108553. https://doi.org/10.1016/j.compositesb.2020.108553.

[3] Rahate AS, Nemade KR, Waghuley SA. Polyphenylene sulfide (PPS): State of the art and applications. Rev Chem Eng 2013;29:471–89. https://doi.org/10.1515/revce-2012-0021.

[4] Zuo P, Tcharkhtchi A, Shirinbayan M, Fitoussi J, Zuo P, Tcharkhtchi A, et al. Overall Investigation of Poly (Phenylene Sulfide) from Synthesis and Process to applications - a Review. Macromol Mater Eng 2020;304:1800686. https://doi.org/10.1002/mame.201800686.

[5] Seki Y, Kizilkan E, Leşkeri BM, Sarikanat M, Altay L, Isbilir A. Comparison of the thermal and Mechanical Properties of Poly(phenylene sulfide) and Poly(phenylene sulfide)-Syndiotactic Polystyrene-based thermal Conductive Composites. ACS Omega 2022;7:45518–26. https://doi.org/10.1021/acsomega.2c06152.

[6] Kumagai S, Sato M, Ma C, Nakai Y, Kameda T. Journal of Analytical and Applied Pyrolysis a comprehensive study into the thermo-oxidative degradation of sulfur-based engineering plastics. J Anal Appl Pyrol 2022;168:105754. https://doi.org/10.1016/j.jaap.2022.105754.

[7] D.G. Brady, H.W. Hill, Polyphenylene Sulfide., in: Eng Thermoplast, 1985: pp. 201–234. https://doi.org/10.1201/b13623-22.

[8] Yoo TJ, Hwang EB, Jeong YG. Thermal and electrical properties of poly(phenylene sulfide)/carbon nanotube nanocomposite films with a segregated structure. Compos A Appl Sci Manuf 2016;91:77–84. https://doi.org/10.1016/j.compositesa.2016.09.022.

[9] Díez-Pascual AM, Naffakh M. Enhancing the thermomechanical behaviour of poly (phenylene sulphide) based composites via incorporation of covalently grafted carbon nanotubes. Compos A Appl Sci Manuf 2013;54:10–9. https://doi.org/10.1016/j.compositesa.2013.06.018.

[10] R.H. Baughman, A.A. Zakhidov, W.A. De Heer, Carbon nanotubes - The route toward applications, Science (80-.). 297 (2002) 787–792. https://doi.org/10.1126/science.1060928.

[11] Singh V, Joung D, Zhai L, Das S, Khondaker SI, Seal S. Graphene based materials: past, present and future. Prog Mater Sci 2011;56:1178–271. https://doi.org/10.1016/j.pmatsci.2011.03.003.

[12] Gao Y, Fu Q, Niu L, Shi Z. Enhancement of the tensile strength in poly(p-phenylene sulfide) and multi-walled carbon nanotube nanocomposites by hot-stretching. J Mater Sci 2015;50:3622–30. https://doi.org/10.1007/s10853-015-8923-2.

[13] Capone C, Di Landro L, Inzoli F, Penco M, Sartore L, Vinci L. Thermal and Mechanical Degradation During Polymer Extrusion Processing 2007:4–10. https://doi.org/10.1002/pen.

[14] Takahashi T, Tsubo S, Inoue K, Suzuki R, Murata H, Tachibana M. Effect of dispersibility of carbon nanotubes on the hardness and thermal properties of polyphenylene sulphide/carbon nanotube composites obtained using solution mixing and melt blending methods. Mater Sci Eng B 2023;295:116579. https://doi.org/10.1016/j.mseb.2023.116579.

[15] Dydek K, Latko-Durałek P, Sulowska A, Kubiś M, Demski S, Kozera P, et al. Effect of processing temperature and the content of carbon Nanotubes on the properties of nanocomposites based on polyphenylene sulfide. Polymers (Basel) 2021;13. https://doi.org/10.3390/polym13213816.

[16] Zhang K, Li GH, Feng LM, Wang N, Guo J, Sun K, et al. Ultralow percolation threshold and enhanced electromagnetic interference shielding in poly(l-lactide)/multi-walled carbon nanotube nanocomposites with electrically conductive segregated networks. J Mater Chem C 2017;5:9359–69. https://doi.org/10.1039/c7tc02948a.

[17] Mohoppu M, Ayan U, Kattel B, Oulhakem O, Villacorta BS. Morphology-driven electromagnetic shielding performance of graphitic nanoparticles in segregated polypropylene nanocomposites via electromagnetic melt processing. Compos Commun 2025;60:102614. https://doi.org/10.1016/j.coco.2025.102614.

[18] M. Mohoppu, U. Ayan, B. Kattel, A. Al-Ostaz, E. Hutchcraft, B.S. Villacorta, 539h - Facile Manufacturing of Recycled Polyphenylene Sulfide-Based Nanocomposites through Novel Electromagnetic Melt-Processing, in: 2024 AIChE Annu. Meet., 2024.

[19] M. Mohoppu, M. Majdoub, S. Nouranian, B. Villacorta, Electromagnetic Processing of Graphitic Nanoparticle-Based Thermoplastic Nanocomposites, in: 2023 AIChE Annu. Meet., AIChE, 2023.

[20] Poyraz S, Zhang L, Schroder A, Zhang X. Ultrafast Microwave Welding/Reinforcing Approach at the Interface of Thermoplastic Materials. ACS Appl Mater Interfaces 2015;7:22469–77. https://doi.org/10.1021/acsami.5b06484.

[21] Potente H, Karger O, Fiegler G. Laser and microwave welding - the applicability of new process principles. Macromol Mater Eng 2002;287:734–44. https://doi.org/10.1002/mame.200290002.

[22] Mohoppu M, Ayan U, Nouranian S, Al-Ostaz A, Ucak-Astarlioglu MG, Villacorta BS. Rapid Microwave Bonding of Thermoplastics Substrates with Electromagnetically Susceptible Graphene/Poly (ether ether ketone) Segregated Nanoformulates. ACS Appl Eng Mater 2025;3:26683. https://doi.org/10.1021/acsaenm.5c00520.

[23] Sgriccia N, Hawley MC. Thermal, morphological, and electrical characterization of microwave processed natural fiber composites. Compos Sci Technol 2007;67: 1986–91. https://doi.org/10.1016/j.compscitech.2006.07.031.

[24] Chaowasakoo T, Sombatsompop N. Mechanical and morphological properties of fly ash/epoxy composites using conventional thermal and microwave curing methods. Compos Sci Technol 2007;67:2282–91. https://doi.org/10.1016/j.compscitech.2007.01.016.

[25] Simunec DP, Jacob J, Kandjani AEZ, Trinchi A, Sola A. Facilitating the additive manufacture of high-performance polymers through polymer blending: a review. Eur Polym J 2023;201:112553. https://doi.org/10.1016/j.eurpolymj.2023.112553.

[26] Mgbemena CO, Li D, Lin MF, Liddel PD, Katnam KB, Kumar VT, et al. Accelerated microwave curing of fibre-reinforced thermoset polymer composites for structural applications: a review of scientific challenges. Compos A Appl Sci Manuf 2018;115: 88–103. https://doi.org/10.1016/j.compositesa.2018.09.012.

[27] Du H, Fang C, Zhang J, Xia X, Weng GJ. Segregated carbon nanotube networks in CNT-polymer nanocomposites for higher electrical conductivity and dielectric permittivity, and lower percolation threshold. Int J Eng Sci 2022;173:103650. https://doi.org/10.1016/j.ijengsci.2022.103650.

[28] Ma Z, Jiang R, Jing J, Kang S, Ma L, Zhang K, et al. Lightweight Dual-Functional Segregated Nanocomposite Foams for Integrated Infrared Stealth and Absorption-Dominant Electromagnetic Interference Shielding. Nano-Micro Lett 2024;16:223. https://doi.org/10.1007/s40820-024-01450-0.

[29] M. Mohoppu, U.R. Ayan, B. Kattel, O. McNair, B. Villacorta, Upcycling of Recycled Polyphenylene Sulfide into Functional High-Performance Nanocomposites Via Novel Electromagnetic Melt-Processing, in: 2025 AIChE Annu. Meet., AIChE, 2025.

[30] Yuan LJ, Mustafa N, Razali N, Hamdan H, Merzeik L. Recycling Polyphenylene Sulfide (PPS): a Comprehensive Review of Mechanical, thermal and Physical Properties for Aerospace Engineering applications. J Kejuruter 2025;37:3827–93. https://doi.org/10.17576/jkukm-2025-37(8)-14.

[31] B. Villacorta, M. Karunarathna, U.R. Ayan, (259h) Next-Generation of Thermoplastic Nanocomposites Via Electromagnetic Processing, in: AIChE Annu. Meet., AIChE, 2022.
[32] Mohoppu M, Ayan U, Schwartz J, Al-Ostaz A, Ucak-Astarlioglu MG, Villacorta BS. Carbon Nanotube-based Segregated Thermoplastic Nanocomposites Structured via Electromagnetic Melt Processing. ACS Omega 2024;9:48546–62. https://doi.org/10.1021/acsomega.4c07372.
[33] Yu WC, Xu JZ, Wang ZG, Huang YF, Yin HM, Xu L, et al. Constructing highly oriented segregated structure towards high-strength carbon nanotube/ultrahigh-molecular-weight polyethylene composites for electromagnetic interference shielding. Compos A Appl Sci Manuf 2018;110:237–45. https://doi.org/10.1016/j.compositesa.2018.05.004.
[34] Yang Z, Peng H, Wang W, Liu T. Crystallization behavior of poly(ε-caprolactone)/layered double hydroxide nanocomposites. J Appl Polym Sci 2010;116:2658–67. https://doi.org/10.1002/app.
[35] Du J, Zhao L, Zeng Y, Zhang L, Li F, Liu P, et al. Comparison of electrical properties between multi-walled carbon nanotube and graphene nanosheet/high density polyethylene composites with a segregated network structure. Carbon N Y 2011;49:1094–100. https://doi.org/10.1016/j.carbon.2010.11.013.
[36] Han MS, Lee YK, Lee HS, Yun CH, Kim WN. Electrical, morphological and rheological properties of carbon nanotube composites with polyethylene and poly (phenylene sulfide) by melt mixing. Chem Eng Sci 2009;64:4649–56. https://doi.org/10.1016/j.ces.2009.02.026.
[37] Liu Z, Peng W, Zare Y, Hui D, Rhee KY. Predicting the electrical conductivity in polymer carbon nanotube nanocomposites based on the volume fractions and resistances of the nanoparticle, interphase, and tunneling regions in conductive networks. RSC Adv 2018;8:19001–10. https://doi.org/10.1039/c8ra00811f.
[38] Forero-Sandoval IY, Franco-Bacca AP, Cervantes-Álvarez F, Gómez-Heredia CL, Ramírez-Rincón JA, Ordonez-Miranda J, et al. Electrical and thermal percolation in two-phase materials: a perspective. J Appl Phys 2022;131. https://doi.org/10.1063/5.0091291.
[39] Bauhofer W, Kovacs JZ. A review and analysis of electrical percolation in carbon nanotube polymer composites. Compos Sci Technol 2009;69:1486–98. https://doi.org/10.1016/j.compscitech.2008.06.018.
[40] Balberg I, Azulay D, Goldstein Y, Jedrzejewski J. Possible origin of the smaller-than-universal percolation-conductivity exponent in the continuum. Phys Rev E 2016;93:1–7. https://doi.org/10.1103/PhysRevE.93.062132.
[41] Park JS, Kim T, Kim WS. Conductive Cellulose Composites with Low Percolation Threshold for 3D Printed Electronics. Sci Rep 2017;7:1–10. https://doi.org/10.1038/s41598-017-03365-w.
[42] Yang J, Xu T, Lu A, Zhang Q, Tan H, Fu Q. Preparation and properties of poly (p-phenylene sulfide)/multiwall carbon nanotube composites obtained by melt compounding. Compos Sci Technol 2009;69:147–53. https://doi.org/10.1016/j.compscitech.2008.08.030.
[43] Ribeiro B, Pipes RB, Costa ML, Botelho EC. Electrical and rheological percolation behavior of multiwalled carbon nanotube-reinforced poly(phenylene sulfide) composites. J Compos Mater 2017;51:199–208. https://doi.org/10.1177/0021998316644848.
[44] Zhang Q, Wang Q, Cui J, Zhao S, Zhang G, Gao A, et al. Structural design and preparation of Ti3C2Tx MXene/polymer composites for absorption-dominated electromagnetic interference shielding. Nanoscale Adv 2023;5:3549–74. https://doi.org/10.1039/d3na00130j.
[45] Bheema RK, Gopu J, Bhaskaran K, Verma A, Chavali M, Etika KC. A review on recent progress in polymer composites for effective electromagnetic interference shielding properties - structures, process, and sustainability approaches. Nanoscale Adv 2024;6:5773–802. https://doi.org/10.1039/d4na00572d.
[46] Hota SS, Panda D, Bhoobash SB, Mishra S, Biswal L, Joshi S, et al. Absorption-Dominant Electromagnetic Interference Shielding of Polymer Nanocomposite PVDF/LiNbO3 for High-Frequency Microwave Application. ACS Appl Electron Mater 2025;7:4481–92. https://doi.org/10.1021/acsaelm.5c00316.
[47] Cui CH, Yan DX, Pang H, Xu X, Jia LC, Li ZM. Formation of a Segregated Electrically Conductive Network Structure in a Low-Melt-Viscosity Polymer for Highly Efficient Electromagnetic Interference Shielding. ACS Sustain Chem Eng 2016;4:4137–45. https://doi.org/10.1021/acssuschemeng.6b00526.
[48] Cheng H, Bai L, Lin G, Zhang X, Wu C, Ma S, et al. Hugely improved electromagnetic interference shielding and mechanical properties for UHMWPE composites via constructing an oriented conductive carbon nanostructures (CNS) networks. J Mater Res Technol 2023;26:6520–31. https://doi.org/10.1016/j.jmrt.2023.08.256.
[49] Zhang L, Yang S, Peng L, Zhong K, Chen Y. Optimized Properties in Multifunctional Polyphenylene Sulfide Composites via Graphene Nanosheets/Boron Nitride Nanosheets dual Segregated Structure under High pressure. Nanomaterials 2022;12:1–19. https://doi.org/10.3390/nano12193543.
[50] Zhang XP, Jia LC, Zhang G, Yan DX, Li ZM. A highly efficient and heat-resistant electromagnetic interference shielding carbon nanotube/poly(phenylene sulfide) composite via sinter molding. J Mater Chem C 2018;6:10760–6. https://doi.org/10.1039/C8TC03493A.
[51] Vovchenko L, Matzui L, Oliynyk V, Milovanov Y, Mamunya Y, Volynets N, et al. Polyethylene composites with segregated carbon nanotubes network: Low frequency plasmons and high electromagnetic interference shielding efficiency. Materials (Basel) 2020;13. https://doi.org/10.3390/ma13051118.
[52] Xie Y, Tang J, Ye F, Liu P. Microwave-Assisted Sintering to Rapidly Construct a Segregated Structure in Low-Melt-Viscosity Poly(Lactic Acid) for Electromagnetic Interference Shielding. ACS Omega 2020;5:26116–24. https://doi.org/10.1021/acsomega.0c03704.
[53] Papageorgiou DG, Li Z, Liu M, Kinloch IA, Young RJ. Mechanisms of mechanical reinforcement by graphene and carbon nanotubes in polymer nanocomposites. Nanoscale 2020;12:2228–67. https://doi.org/10.1039/c9nr06952f.
[54] Rezzig D, Tarfaoui M, Abdeslam S. The effect of interphase and agglomeration on the mechanical properties of aluminum matrix nanocomposites reinforced with carbon nanotubes. Mater Today Commun 2023;37. https://doi.org/10.1016/j.mtcomm.2023.107103.
[55] Nurazzi NM, Sabaruddin FA, Harussani MM, Kamarudin SH, Rayung M, Asyraf MRM, et al. Mechanical Performance and applications of CNTs Reinforced Polymer Composites — a Review. Nanomater Rev 2021;11:2186. https://doi.org/10.3390/nano11092186.
[56] Ayan U, Mohoppu M, Sebastian JA, Shreyan BR, Toragall VB, Maniruzzaman M, et al. Polylactic Acid / Polybutylene Adipate Terephthalate-Carbon Nanotube Nanobiocomposites with a Segregated Toughening Morphology Yielding Large Ductility for Biocompatible Materials. ACS Appl Nano Mater 2025;8:1537–56. https://doi.org/10.1021/acsanm.4c06353.
[57] Pandey G, Thostenson ET. Carbon Nanotube-based Multifunctional Polymer Nanocomposites. Polym Rev 2012;52:355–416. https://doi.org/10.1080/15583724.2012.703747.
[58] Salah N, Alfawzan AM, Saeed A, Alshahrie A, Allafi W. Effective reinforcements for thermoplastics based on carbon nanotubes of oil fly ash. Sci Rep 2019;9:1–13. https://doi.org/10.1038/s41598-019-56777-1.
[59] Wang B, Li N, Liu Z, Bao Q, Cheng S, Feng J, et al. Research on the thermal conductivity and mechanical properties of carbon fiber reinforced thermoplastic composites doped with different sizes carbon nanotubes: a combination of experiments, numerical simulations and multi-objective optimization. Polym Compos 2024;45:11252–65. https://doi.org/10.1002/pc.28563.
[60] Sevriugina V, Pavliňák D, Ondreáš F, Jašek O, Štaffová M, Lepcio P. Matching Low Viscosity with Enhanced Conductivity in Vat Photopolymerization 3D Printing: Disparity in the Electric and Rheological Percolation Thresholds of Carbon-based Nanofillers is Controlled by the Matrix Type and Filler Dispersion. ACS Omega 2023;8:45566–77. https://doi.org/10.1021/acsomega.3c05683.
[61] Arrigo R, Malucelli G. Rheological behavior of polymer/carbon nanotube composites: an overview. Materials (Basel) 2020;13:1–27. https://doi.org/10.3390/ma13122771.
[62] Nadiv R, Fernandes RMF, Ochbaum G, Dai J, Buzaglo M, Varenik M, et al. Polymer nanocomposites: Insights on rheology, percolation and molecular mobility. Polymer (Guildf) 2018;153:52–60. https://doi.org/10.1016/j.polymer.2018.07.079.
[63] Zelelew TM, Ali AN, Kidanemariam G, Kebede GA, Koricho EG. The effect of Nanoparticle Reinforcement on Shear-Thickening Fluid. J Nanotechnol 2024;2024:1–18. https://doi.org/10.1155/2024/8819920.
[64] Hilarius K, Lellinger D, Alig I, Villmow T, Pegel S, Pötschke P. Influence of shear deformation on the electrical and rheological properties of combined filler networks in polymer melts: Carbon nanotubes and carbon black in polycarbonate. Polymer (Guildf) 2013;54:5865–74. https://doi.org/10.1016/j.polymer.2013.08.010.
[65] Majumdar S, Krishnaswamy R, Sood AK. Discontinuous shear thickening in confined dilute carbon nanotube suspensions. PNAS 2011;108:8996–9001. https://doi.org/10.1073/pnas.1018685108.
[66] Obrzut J, Douglas JF, Kharchenko SB, Migler KB. Shear-induced conductor-insulator transition in melt-mixed polypropylene-carbon nanotube dispersions. Phys Rev B - Condens Matter Mater Phys 2007;76:1–9. https://doi.org/10.1103/PhysRevB.76.195420.
[67] Oseli A, Vesel A, Žagar E, Perše LS. Mechanisms of Single-Walled Carbon Nanotube Network Formation and its Configuration in Polymer-based Nanocomposites. Macromolecules 2021;54:3334–46. https://doi.org/10.1021/acs.macromol.0c02763.
[68] Achilias DS. Polymer degradation under microwave irradiation. Adv Polym Sci 2016;274:309–46. https://doi.org/10.1007/12_2014_292.
[69] Dörr D, Kuhn U, Altstädt V. Rheological study of gelation and crosslinking in chemical modified polyamide 12 using a multiwave technique. Polymers (Basel) 2020;12:7–9. https://doi.org/10.3390/POLYM12040855.
[70] Verma P, Verma M, Gupta A, Chauhan SS, Malik RS, Choudhary V. Multi walled carbon nanotubes induced viscoelastic response of polypropylene copolymer nanocomposites: effect of filler loading on rheological percolation. Polym Test 2016;55:1–9. https://doi.org/10.1016/j.polymertesting.2016.08.001.
[71] Ke K, Wang Y, Luo Y, Yang W, Xie BH, Yang MB. Evolution of agglomerate structure of carbon nanotubes in multi-walled carbon nanotubes/polymer composite melt: a rheo-electrical study. Compos B Eng 2012;43:3281–7. https://doi.org/10.1016/j.compositesb.2012.02.011.